Materials Chemistry and Physics 146 (2014) 512–522

Contents lists available at ScienceDirect

Materials Chemistry and Physics

journal homepage: www.elsevier.com/locate/matchemphys

Tool wear and its effect on microstructure and properties of friction stir processed Ti–6Al–4V

L.H. Wu, D. Wang, B.L. Xiao, Z.Y. Ma*

Shenyang National Laboratory for Materials Science, Institute of Metal Research, Chinese Academy of Sciences, 72 Wenhua Road, Shenyang 110016, China

HIGHLIGHTS

- Ti–6Al–4V was subjected to friction stir processing by pcBN tool.
- Tool wear was systematically studied under different tool rotation rates.
- Main wear product was TiB phase coming from phase sequences BN–TiB_2–TiB–Ti (N).
- Tool wear led to the increment in hardness and strength but the loss of ductility.

ARTICLE INFO

Article history:
Received 3 June 2013
Received in revised form
17 March 2014
Accepted 3 April 2014

Keywords:
Electron microscopy
Alloys
Wear
Microstructure
Mechanical properties
Phase transitions

ABSTRACT

Ti–6Al–4V alloy was subjected to friction stir processing at rotation rates of 400, 800 and 1200 rpm using a polycrystalline cubic boron nitride (pcBN) tool and tool wear at different travel distances was investigated. At high rotation rates of 800 and 1200 rpm, the greatest tool wear, including mechanical and chemical wear, occurred at the initial tool plunge point. Detailed microstructural examinations on the tool plunge point at 1200 rpm by transmission electron microscopy indicated that the "onion ring" structure in the stir zone was caused by a variation in the distribution of TiB particles. Two similar but not identical spatial phase sequences around BN particles, BN–TiB_2–TiB–α-Ti (N) and BN–TiB_2–TiB –transformed β-Ti (N), as well as Ti2N phase were identified. The reaction mechanism between the tool and the Ti matrix was discussed. Moreover, when the tool wear reached a steady-state condition, the effect of tool wear on the microstructure and mechanical properties of the stir zone was evaluated. A fully transformed β with a Widmanstatten structure was observed at all rotation rates and the average size of prior β grains increased with the rotation rate. The tool wear led to an increment in hardness and tensile strength but a loss of ductility of the stir zone.

1. Introduction

Titanium and its alloys have been extensively applied in aerospace, chemical and biomedical fields because of their high specific strengths, excellent corrosion resistance and good compatibility [1]. Ti–6Al–4V is the most widely used α + β titanium alloy and occupies over 50% of the total titanium market [1]. The welding of Ti–6Al–4V is extensively applied to join large or complex structural components in various industries. However, there are some obvious limitations associated with conventional fusion welding of wrought Ti–6Al–4V, such as microstructural and mechanical behavior discontinuity, epitaxial growth and coarse beta grains, and a significant distortion with a high residual stress [1]. To avoid these issues associated with melting and solidification of welded materials, solid-state welding techniques such as friction stir welding (FSW) appear to more suitable for joining titanium alloys.

Friction stir welding (FSW) has attracted great attention in the industrial world due to its many advantages since its invention in 1991 [2,3] and it has been widely studied and used in commercial low-melting-temperature alloys, such as aluminum and magnesium alloys [4–7]. In recent years, the feasibility of FSW of high-melting-temperature alloys such as titanium alloys has been investigated. It was reported that high-quality welds of titanium alloys without any defects could be obtained by FSW and the joint efficiency could be over 90% [8,9].

However, compared to low-melting-temperature alloys, the research on the FSW of titanium alloys is still limited mainly because of two issues. The first one is a limited FSW process window for

* Corresponding author. Tel./fax: +86 24 83978908.
E-mail address: zyma@imr.ac.cn (Z.Y. Ma).

http://dx.doi.org/10.1016/j.matchemphys.2014.04.002
0254-0584/

obtaining defect-free joints due to low thermal conductivity and bad forming ability of titanium alloys. For example, Edwards and Ramulu [10] reported that the FSW process window of Ti–6Al–4V alloy was very narrow (~150–400 rpm in rotation rate and 75–125 mm min^{-1} in travel speed). The second one is a lack of suitable tools. The requirement for the tool is high resistance to wear, high strength and hardness at both room and elevated temperatures, and effective heat-dissipation ability during FSW process.

W-series alloys such as W alloys and WC materials have been mainly used as the tool materials for FSW of titanium alloys [10–13]. TiC and Mo-based alloys have also been reported as tool materials for FSW of titanium alloys [14,15]. Unfortunately, for all these tools, tool wear seems inevitable due to the high strength/hardness and high welding temperature of titanium alloys. For example, Pilchak et al. [12] showed that millimeters of bands consisted of sub-micro-sized tungsten-rich particles as the result of tool wear were deposited in the stir zone. Tool wear will not only reduce the lifetime of the tool but also probably affect the material flow and the properties of the welds.

Polycrystalline cubic boron nitride (pcBN), which is used as a cutting tool for steels [16] and Ti alloys [17], has shown the feasibility as the FSW tool for high melting temperature alloys such as steels [18–20], and defect-free welds could be obtained [18,20]. Zhang et al. [21] conducted a preliminary study on FSW of pure Ti using pcBN tool, and microstructure and property investigations showed that pcBN has the potential as the tool of FSW for pure Ti, although tool wear was observed in the weld. However, there are no reports on feasibility of FSW of titanium alloys such as Ti–6Al–4V using pcBN tool. It is probably more challenging for FSW of Ti–6Al–4V, because of its higher strength and welding temperature and worse plasticity.

In the past few years, several investigations on tool wear of pcBN in the FSW steel welds [22,23] have been reported. For example, Park et al. [22] conducted a detailed study on the tool wear in FSW stainless steel welds using pcBN tool. They reported that apart from mechanical wear, chemical wear occurred and Cr-rich borides formed through the reaction between the workpiece and the pcBN tool. For FSW of titanium and its alloys, however, only Zhang et al. [21] succinctly reported tool wear of pcBN during FSW of pure Ti using EMPA and EDS and they inferred that BN might have reacted with Ti. However, how the FSW parameters influenced tool wear and the nature of the wear products remain unknown so far.

In order to evaluate the suitability of pcBN tools for FSW of titanium alloys, it is of practical importance to systematically examine tool wear under different parameters. It is also of great significance to clarify the nature of wear products of pcBN tools and to check whether B or/and N exist only in the form of BN or indeed react with the elements in titanium alloys to form other compounds. Furthermore, investigation of this subject can also provide some fundamental knowledge about the wear of pcBN tools for cutting titanium alloys [17] and the interface reaction between BN and titanium alloys when BN is used for ceramic parts such as the crucibles that interact directly with titanium alloys at high temperature [24].

Although the previous studies on the FSW of composites showed that tool wear significantly deteriorated properties of the welds [25], no such results have been reported in the friction stir welds of titanium alloys. Therefore, it is necessary to examine whether and how tool wear influence the properties of the welds of titanium alloys since there is inevitable tool wear in the welds.

In the current study, Ti–6Al–4V was friction stir processed (FSP) using a pcBN tool over a wide range of rotation rates from 400 to 1200 rpm, and tool wear and the microstructure and mechanical properties of the stir zones were examined. Based on the similar principle of FSW and FSP, the FSP sample essentially represents a bead-on-plate (no seam) weld, and tool wear and microstructure and properties in the stir zone for the FSP samples are the same as that for the FSW samples. Therefore, it is appropriate to use FSP to represent FSW to achieve the purpose of this study. The objective of this study is (a) to clarify the nature of wear products of pcBN tool and their effect on microstructure and properties and (b) to exploit a larger FSW window using a pcBN tool.

2. Experimental procedure

Four-millimeter-thick commercial mill-annealed Ti–6Al–4V plate was used as the raw material. The plate was friction stir processed along the rolling direction at a constant travel speed of 100 mm min^{-1} with various rotation rates of 400, 800 and 1200 rpm. A pcBN tool with a shoulder 15 mm in diameter and a triangular prismatic pin 6 mm in diameter and 2.2 mm in length was used. Argon shielding was employed to prevent oxidation of the plate surface.

Fig. 1 shows macro- and microstructure observation locations away from the tool plunge point for investigating tool wear. Microstructural characterization and analysis were conducted using optical microscopy (OM), scanning electron microscopy (SEM, Supra 55) and transmission electron microscopy (TEM, FEI, Tecnai G^2 20) with an energy-dispersive spectroscope (EDS, Oxford). The EDS experiments were operated on SEM and TEM with accelerating voltages of 20 kV and 200 kV, respectively. The OM and SEM specimens were etched in Kroll's reagent. The prior β grain size of the FSP samples was estimated by the linear inception method, and more than 400 grains were measured. Thin films for TEM were mechanically polished to ~30 μm. In order to locate the region of the wear products precisely, thin films were etched in Kroll's reagent before being punched into 3 mm discs, dimpled to ~10 μm, and finally thinned to perforation by the ion-milling technique.

Mini-tensile specimens with a gauge length of 5.0 mm, a width of 1.4 mm and a thickness of 0.8 mm were cut from the base metal (BM) and the SZ of the FSP plate perpendicular to the processing direction. Tensile test was performed at room temperature at a strain rate of 10^{-3} s^{-1}. Vickers hardness measurement was conducted using a Vickers indent with a load of 300 g and a dwell time of 15 s.

In this work, the specimen cut from the location *M* mm away from the plunge point of the FSP plate at a rotation rate of *N* rpm will be simplified as *N* rpm–*M* mm specimen. For example, the specimen cut from the location 7 mm away from the plunge point of the FSP plate at 400 rpm is denoted by 400 rpm–7 mm specimen.

3. Results

3.1. Macrostructural evolution as travel distance increased at different rotation rates

Fig. 2 shows the cross-section macrographs of 400 rpm FSP sample at different travel distances. All the SZs showed a parabolic

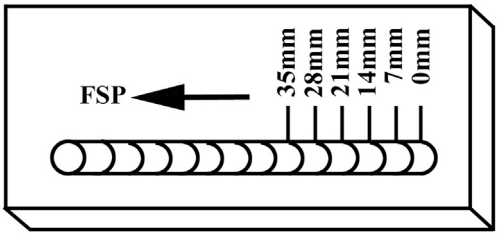

Fig. 1. Cross-section observation locations in FSP samples.

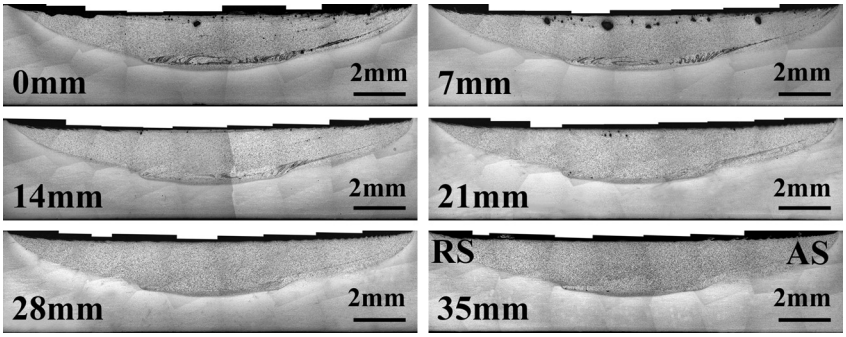

Fig. 2. Cross sections of 400 rpm FSP sample at different travel distances away from the tool plunge point.

profile. Near the top surface of the 400 rpm–0 mm specimen, black particles with sizes of about 1–100 μm were observed and as the travel distance increased, the number of these black particles increased at first (travel distance less than 7 mm) and then decreased until they almost disappeared at a travel distance of about 28 mm. At the bottom of the SZ, there were black bands with deeply etched lines and as the distance increased, the contrast of these bands became weaker and weaker until they disappeared.

EDS analysis showed that the blocky black particles near the top surface mainly contained B and N elements (Fig. 3(a)) and the matrix in the SZ contained 5.8 wt.% Al, 3.7 wt.% V and 90.5 wt.% Ti, which suggested that these black particles were pcBN tool wear debris. In black bands at the bottom of the SZ, a number of fine rod-shaped white particles were observed in an equiaxed $\alpha +$ transformed β, i.e. bimodal matrix (Fig. 3(b)). These rod-shaped white particles should be related to tool wear products and will be studied in detail in the next part. In these bands, the microstructure was obviously different from that in other regions of the SZ where there was no tool wear and a Widmanstatten structure was observed (Fig. 3(c)).

Fig. 4 shows the cross-section macrographs of 800 rpm FSP sample at different travel distances. Macrographs for all travel distances were similar which were characterized by band structures with deeply etched lines near the top surface and in the middle of the parabolic-shaped SZ. As the travel distance increased, the band contrast showed a trend of gradually becoming weak and then remaining unchanged. In these bands, BN particles and fine rod-shaped white particles, similar to those in 400 rpm–0 mm specimen, could also be found. Typical microstructures of the SZ in 800 rpm–0 mm specimen were shown in Fig. 5. Obviously, the microstructure in the dark bands also showed a difference from that in other regions where there was no tool wear.

Fig. 6 shows the cross-section macrographs of 1200 rpm FSP sample at different travel distances. In all the cross-section macrographs, there was also a band near the top surface, like that in 800 rpm FSP sample. In 1200 rpm–0 mm specimen, an "onion ring" structure that was commonly observed in FSW aluminum alloy welds was found. As the travel distance increased, the "onion ring" contrast became weaker and after a travel distance of about 14 mm, the contrast hardly changed and only obscure outlines were observed. Obviously, 1200 rpm–0 mm specimen showed an interesting "onion ring" structure which may be related to tool wear. In the previous investigations, no such "onion ring" structure was reported in FSW/FSP titanium alloys [8,14]. Therefore in the

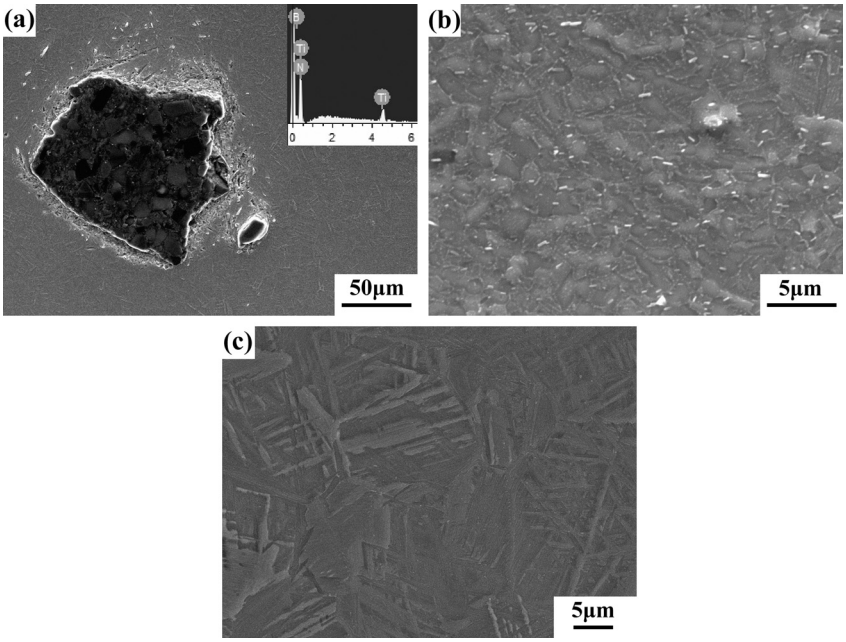

Fig. 3. SEM images of the SZ in 400 rpm–0 mm specimen: (a) near the top surface with an inserted EDS spectrum of the blocky particle, (b) in black bands of the SZ in the bottom, and (c) in the region where there was no tool wear.

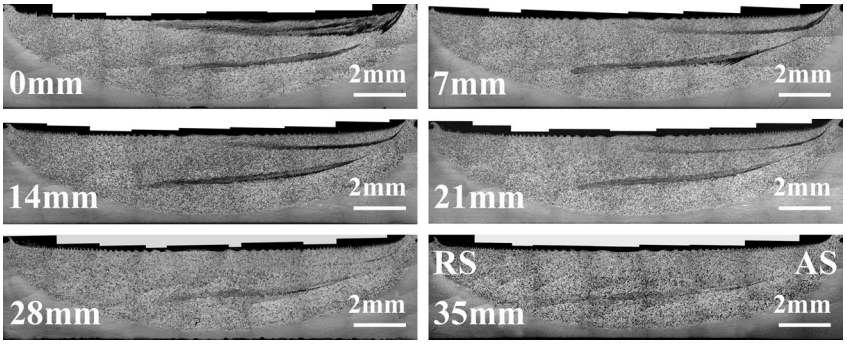

Fig. 4. Cross sections of 800 rpm FSP sample at different travel distances away from the tool plunge point.

following part, 1200 rpm–0 mm specimen will be examined in detail to clarify the nature of unknown second-phase particles and their formation mechanism.

3.2. Microstructure characterization in 1200 rpm–0 mm specimen

Magnified optical macrograph in Fig. 7(b) and SEM image in Fig. 7(c) show the "onion ring" structure more clearly. Detailed microstructural examinations of 1200 rpm–0 mm specimen showed that there were three types of microstructures in the SZ. The first type was a Widmanstatten structure, as shown in Fig. 7(d), which existed in bright regions of the SZ (D in Fig. 7(a)) and the bright bands of the "onion ring" structure.

The second type of microstructure was in the dark bands of the "onion ring" region, where large quantities of rod-shaped white particles (50–300 nm in width and 0.2–2 μm in length) were observed in a Widmanstatten matrix (Fig. 7(e)). Besides, a core–shell structure, consisting of a large black particle core (several micrometers in size) with white particle layers around it, was also observed (Fig. 7(e)). EDS analyses indicated that the large black particle core contained 48.6 wt.% B and 51.4 wt.% N, and the matrix contained 5.9 wt.% Al, 3.8 wt.% V and 90.3 wt.% Ti. The compositions of the black particles were very close to those of the BN phase, suggesting that they were tool wear debris. The magnified image in Fig. 7(f) shows that such a core–shell structure contained three layers: the BN core, the second layer, consisting of large numbers of ~20 nm spherical particles, and the third layer, consisting of rod-shaped particles (50–300 nm in width and 0.2–2 μm in length). These rod-shaped particles exhibited a clear trend of being swept into the matrix. Therefore, the rod-shaped particles in the matrix probably came from the third layer of the core–shell structure due to material flow.

The third type of microstructure came from the dark band (rectangle E in Fig. 7(a)), which looked like the tail of the "onion ring" region. For the simplification, we called this band the "tail band". In this band, large quantities of fine rod-shaped white particles were homogeneously distributed in the matrix (Fig. 8(a) and (b)). Besides, there were many disc-shaped "reliefs" with sizes from 1 to 10 μm, which tended to "bubble" from the matrix. These "reliefs" could be classified into three types on the basis of different cores, corresponding to three types of core–shell structures, and were marked with 1, 3 in Fig. 8(a) and 2 in Fig. 8(b), respectively.

The first type of core–shell structure (marked with 1 in Fig. 8(a)) contained four layers: three inner layers, similar to the BN core–shell structure in the "onion ring" region in Fig. 7(f), and a disc-shaped external layer, whose magnification is shown in Fig. 8(c). In other words, the BN core–shell structure in the "tail band" contained one more layer than that in the "onion ring" region. The second type (marked with 2 in Fig. 8(b)) contained an inner layer, consisting of fine rod-shaped white particles, whose magnification is shown in Fig. 8(d), and a disc-shaped external layer. The third type (marked with 3 in Fig. 8(a)) contained only a disc-shaped layer. Strictly speaking, the third type should not be called a core–shell structure, but here, it is just for convenience when explaining the reaction process between Ti and BN in the subsequent text.

TEM examinations of the dark bands in the "onion ring" region and the "tail band" revealed the existence of several tens to hundreds of nanometers-sized particles with various shapes including rod, regular and irregular hexagonal morphologies. These different shaped particles were composed of the same elements and crystal structure, and could be identified as the same phase by selected-area diffraction (SAD). Typical TEM images of the rod-shaped particle, with inserted SAD with [100] and [10-1] zone axis patterns and an EDS image, and the hexagonal particle are shown in Fig. 9(a) and (b), respectively. In Fig. 9(a), a boron peak was clearly observed in the EDS and this particle was identified as TiB phase by the SAD patterns. TiB is orthorhombic, space group Pnma with the lattice parameters $a = 6.123$ Å, $b = 3.060$ Å

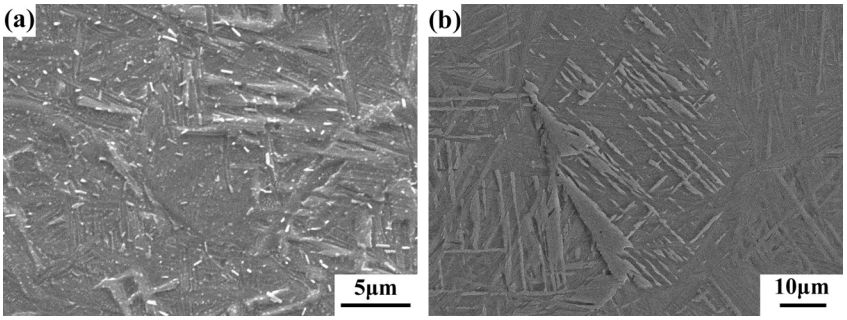

Fig. 5. SEM images of (a) fine rod-shaped white particles in black bands, and (b) the matrix of the SZ where there was no tool wear in 800 rpm–0 mm specimen.

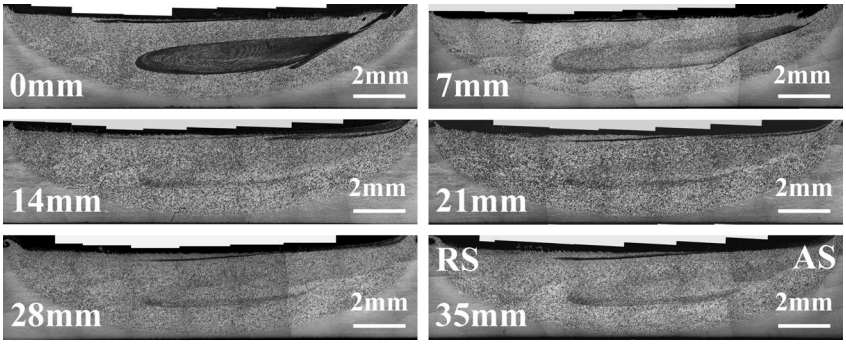

Fig. 6. Cross sections of 1200 rpm FSP sample at different travel distances away from the tool plunge point.

and $c = 4.560$ Å. TiB particles usually exhibit three-dimensional hexagonal prism-shaped and observed TiB particles with different shapes are believed to be related to different cross sections of hexagonal prism TiB particles.

Besides, in many TiB particles, stacking faults on the (100) crystallographic plane were observed (Fig. 9(c)). This feature was commonly reported in TiB particles in the previous study [26]. Moreover, some ~1 μm spherical particles could sometimes be detected in the SZ, and were identified as Ti2N by SAD (Fig. 9(d)). Ti2N is tetragonal, space group P42/mnm with the lattice parameters $a = 4.945$ Å and $c = 3.034$ Å.

TEM examinations of different core–shell structures in the "tail band" confirmed that the rod-shaped particles in the third layer of the first type of core–shell structure and in the core of the second type of core–shell structure were the same phase as those in the matrix, that is, TiB phase. The most external disc-shaped layers of the three types of core–shell structures were identified as the same phase. Typical TEM images of the first type of core–shell structure are shown in Fig. 10. The core was identified as BN phase by SAD, which confirmed the previous inference from EDS, and the nanometer-sized particles in the second layer were identified as TiB_2 by SAD (Fig. 10(a)). TiB_2 is hexagonal, space group P6/mmm with the lattice parameters $a = 3.036$ Å and $c = 3.238$ Å. The rod-shaped particles in the third layer were TiB. The most external layer was identified as α-Ti by SAD (Fig. 10(b)). In the α-Ti layer, N element could be detected by EDS analysis (not shown), suggesting that N was dissolved into α-Ti to form an α-Ti (N) layer.

Therefore, the first type of core–shell structure in the "tail band" consisted of a BN core and TiB_2, TiB, and α-Ti (N) layers from the center to the outside. The second type consisted of TiB particles core and an α-Ti (N) layer. The third type had an α-Ti (N) layer. The BN core–shell structure in the "onion ring" region contained BN core, TiB_2 layer, TiB layer and in the outside, there was a transformed β matrix.

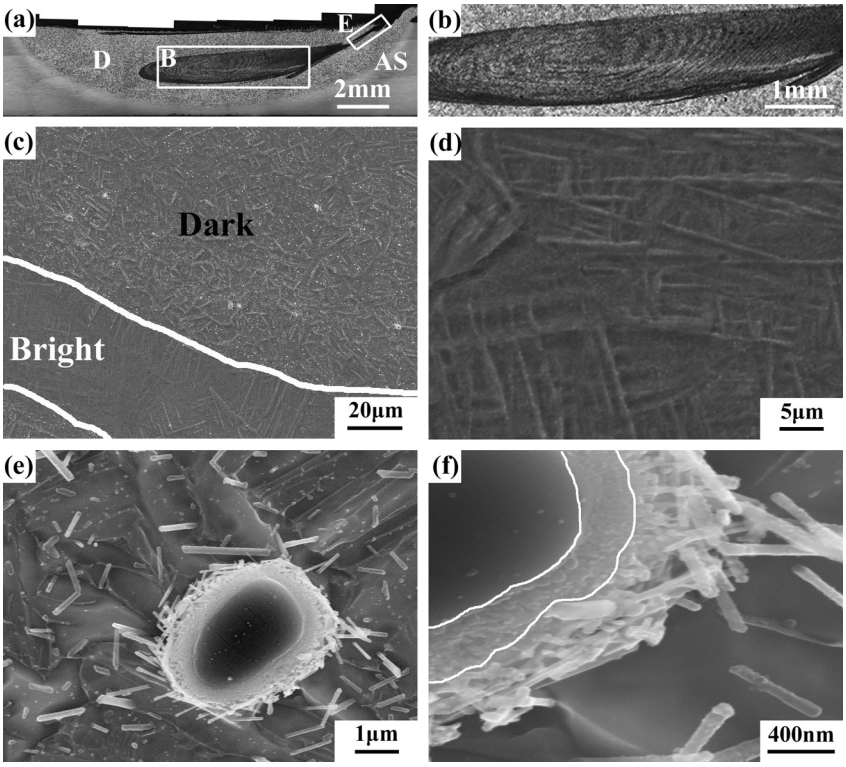

Fig. 7. Optical microstructure of 1200 rpm–0 mm specimen: (a) cross-section, (b) magnification of "onion ring" in rectangle B in (a), and SEM images showing (c) microstructure of bright and dark bands of "onion ring", (d) Widmanstatten structure in D region in (a), (e) microstructure in dark bands of the "onion ring" region, and (f) magnification of core–shell structure in (e).

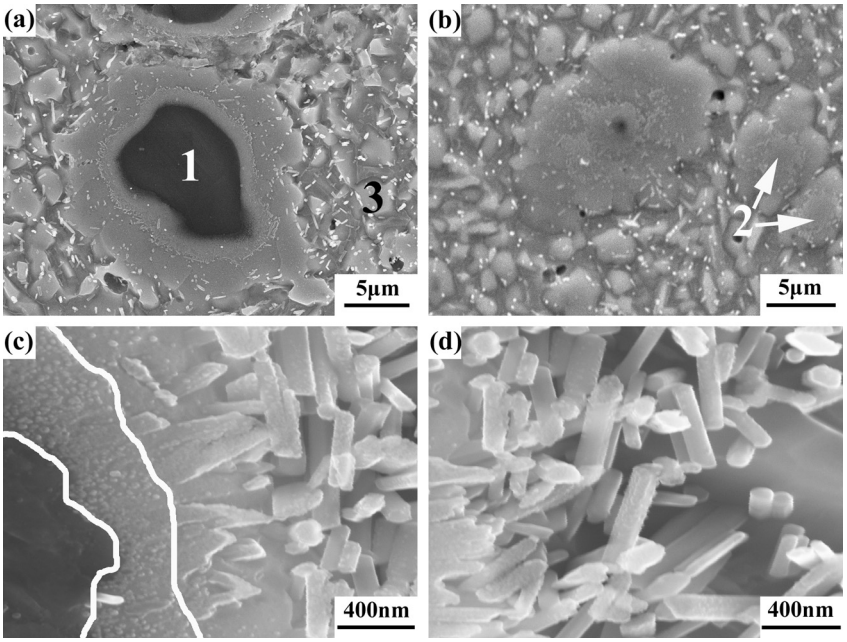

Fig. 8. (a), (b) microstructure in rectangle E in Fig. 7(a), and (c), (d) magnification of the first type and the second type of core–shell structures in (a) and (b), respectively.

3.3. Microstructure and properties of the SZs at different rotation rates

Based on the microstructural observations in Section 3.1, the tool wear at all rotation rates reached a steady-state condition at a travel distance of ~28 mm, therefore, in this part, the specimens for investigating the microstructure and properties were cut from the locations over 50 mm from the plunging point, where the processing forces were also believed to reach normally steady-state conditions [12].

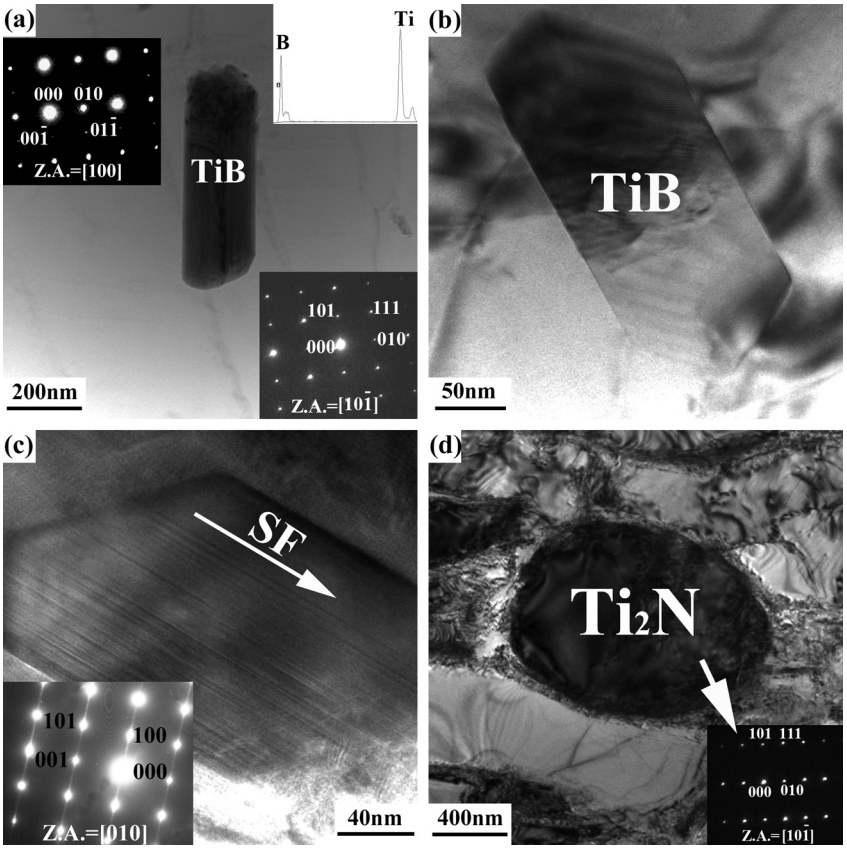

Fig. 9. TEM images of TiB phase with (a) a rod-shape with inserts showing SAD with two different zone axis patterns and an EDS image, (b) a hexagonal shape, (c) stacking faults, and (d) Ti2N phase.

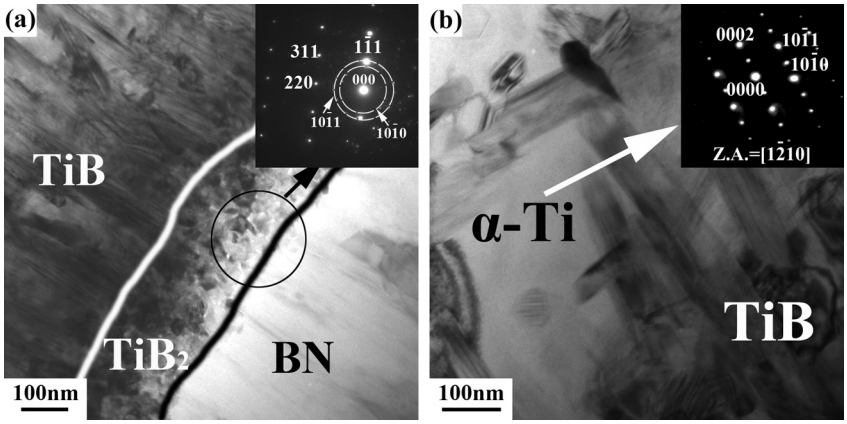

Fig. 10. (a) BN core–shell structure in the "tail band" with an inserted SAD pattern of BN and nanometer TiB_2 particles, and (b) α-Ti layer.

Fig. 11 shows the cross-section macrographs in the locations about 75 mm from the plunging point at different rotation rates. The SZ in each FSP sample exhibited a parabolic shape and the SZ broadened as the rotation rate increased. In each cross-section, four distinct regions could be observed, which were named the SZ, TMAZ, HAZ and BM, as marked in Fig. 11. In the 400 rpm FSP sample, cavities were found at the bottom of the SZ. In the 800 rpm and 1200 rpm samples, no defects except for wear bands were found.

Microstructures of the BM, HAZ and TMAZ of the 800 rpm FSP sample are shown in Fig. 12. The BM (Fig. 12(a)) consisted of equiaxed primary α ($\alpha_p \sim 3$ μm) with the transformed β (whose magnified image was shown in the insert) located at the "triple-points" of the α grains, which is usually called fully equiaxed microstructure. The microstructure in the HAZ (Fig. 12(b)) changed into an equiaxed primary α with a volume fraction of about 50% and transformed β (lamellar secondary α + residual β), that is, so-called bimodal microstructure. This change originated from that β phase increased its volume fraction due to the temperature rise and then was transformed into lamellar secondary α and residual β during the subsequent cooling. In the TMAZ, due to higher temperature and deformation, the volume fraction of primary α decreased rapidly to less than 5%. Therefore the TMAZ consisted of transformed β and a small number of primary α (Fig. 12(c)).

SEM images showed that the SZs in all rotation rates consisted of fully transformed β with a Widmanstatten structure and prior β grains were decorated by fine grain boundary α marked with white lines (Fig. 13(a)–(c)). The average size of the prior β grains increased with the rotation rates and they were 22, 47 and 56 μm at rotation rates of 400, 800 and 1200 rpm, respectively.

In the bands with wear particles of the SZs at 800 and 1200 rpm, the size of prior β grains was similar to that in regions where there was no tool wear. Typical microstructure in the wear band of the 1200 rpm FSP sample is shown in Fig. 13(d) and (e). In this region, fine rod-shaped TiB particles but no BN particles or core–shell structures were observed. Besides, the number of α variants increased and the length of α variants decreased largely compared with that in the SZ where there was no wear particle at 1200 rpm (Fig. 13(c).

Vickers hardness in different regions at different rotation rates is shown in Table 1. The HAZs or TMAZs in all the FSP samples were the lowest hardness region. The SZ at 400 rpm showed a slightly higher hardness than that at 800 and 1200 rpm. The hardness in the wear bands of the SZs showed a little increment compared with that in regions where there was no tool wear.

Tensile properties of the SZs at different rotation rates are shown in Table 2. All the SZs showed a slightly lower tensile strength and ductility than the BM. The tensile specimens containing the wear bands at both 800 and 1200 rpm showed a higher strength but a lower ductility than those without wear bands. There were 20% and 32% losses of ductility in the tensile specimens containing wear bands at 800 and 1200 rpm, respectively.

4. Discussion

4.1. Tool wear at different rotation rates

At all rotation rates, tool wear including mechanical wear and chemical wear occurred (Figs. 2, 4 and 6). This phenomenon was also found in FSW stainless steel joints using pcBN tool [22]. It was reported that the greatest forces would be reached at the initial tool plunge stage during FSW of titanium alloys [27]. Therefore, in this study, at higher rotation rates of 800 and 1200 rpm, the greatest tool wear occurred at the initial tool plunge stage probably because of the greatest forces in this stage.

At 400 rpm, however, the greatest tool wear was not observed at the plunge point. The blocky wear particles including several single cBN particles were detected at the plunge point at 400 rpm because of insufficient heat input. Blocky wear debris was peeled off from the tool, which probably deteriorated the wear-resistance

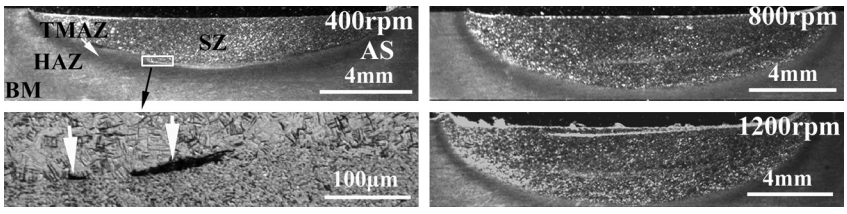

Fig. 11. Cross-section macrographs with a travel distance of about 75 mm at different rotation rates and defects marked by white arrows at the bottom of the SZ in 400 rpm FSP sample.

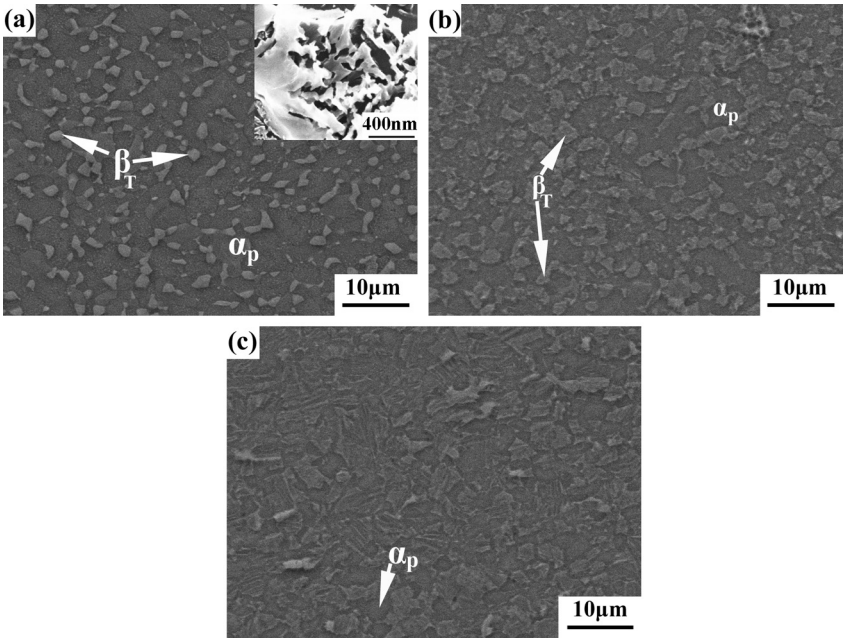

Fig. 12. SEM images of (a) base material, (b) HAZ, and (c) TMAZ of 800 rpm FSP sample. β_T represented the transformed β.

of the tool and thereby greater tool wear occurred in the subsequent travel process. As the travel distance increased, the processing temperature increased, which decreased the trend that BN particles were peeled off from the tool. It was reported that a self-optimized geometrical shape of the tool could be obtained in the FSW joints of ceramic particle reinforced Al matrix composites as the travel distance increased [28]. In this study, the shape optimization effect of the tool was also likely to take place. Therefore, the greatest tool wear occurring at the position 7 mm from the plunge point should be the combination of the factors mentioned above.

4.2. Reaction mechanism between Ti and BN in 1200 rpm–0 mm specimen

An "onion ring" structure was evidently visible in the 1200 rpm–0 mm specimen (Fig. 7(a)). In the previous studies of FSW Al alloys, the "onion ring" structure was considered to be related to geometrical effect [29], the variations of grain sizes and distribution of the second-phase particles [30], and the variation of texture components [31]. In this study, the "onion ring" structure was related to the variations of spatial distribution of the TiB second-phase particles (Fig. 7(c)), which were caused by the reaction between pcBN tool and Ti.

It is known that different reaction products between BN and Ti could be obtained dependent on the reaction condition and the proportion of the reagents. In this study, core–shell structure in the "onion ring" region and the "tail band" (Figs. 7 and 8) clearly indicated that different reaction layers were obtained. The different core–shell structures in the "tail band" should correspond to different intermediate reaction products between Ti and BN. Based on the different reaction products, the reaction mechanism of Ti and BN is proposed as follows (Fig. 14).

(1) In the initial stage (Fig. 14(a)), Ti was rapidly softened and stuck to BN particles at high temperature. The peak temperatures of the welding tool were reported to exceed 1300 °C when Ti–6Al–4V was friction-stir welded at a rotation rate of 800 rpm [12]. The peak welding temperature usually increases with the rotation rate, though it is also influenced by other factors such as tool material, tool geometry, plate thickness, and so on. In this study, FSP was conducted at a rotation rate of 1200 rpm, and it is very likely that the peak temperature exceeded 1300 °C in the SZ.

(2) In reaction stage 1 (Fig. 14(b)), a TiB_2 layer around the BN particle and an α-Ti (N) layer outside were formed. Due to the high affinity between Ti and both B and N, the reaction products between Ti and BN could be titanium boride or/and nitride. TiB_2 is the most stable compound when the temperature is over ~800 K because the Gibbs free energy of its formation is minimal compared with other compounds [32]; therefore, Ti reacted firstly with B to form TiB_2; that is, $Ti + 2BN \rightarrow TiB_2 + 2[N]$. The released N atoms diffused toward the Ti matrix to form an α-Ti (N) layer because of their high solubility in α-Ti (Fig. 15).

(3) In reaction stage 2 (Fig. 14(c)), BN was further consumed and a TiB layer formed. At this reaction stage, Ti and TiB_2 further reacted at the α-Ti/TiB_2 interface to form a TiB layer due to the small negative Gibbs free energy of the reaction: $Ti + TiB_2 \rightarrow 2TiB$ [32]. During the reaction, B atoms diffused from TiB_2 toward α-Ti (N) and reacted with Ti at the TiB/α-Ti (N) interface, which was believed to control the growth of the TiB layer [33]. Obviously the new TiB layer separated TiB_2 and α-Ti (N) and thus became the "barrier layer" of B diffusion. However, this "barrier layer" was subsequently broken up by the severe plastic deformation during FSP and TiB particles flowed into the matrix, which reduced the thickness of the "barrier layer" and accelerated the diffusion rate of B, thus accelerated the growth of TiB. Besides, Ti atoms diffused toward BN and reacted with BN at the TiB_2/BN interface to form TiB_2; that is, $Ti + 2BN \rightarrow TiB_2 + 2[N]$, leading to further consumption of BN. Obviously for most BN particles the reaction stopped at this reaction stage because of the short reaction time during FSP, and a spatial phase sequence of BN–TiB_2–TiB–α-Ti (N) was finally observed (the first type of core–shell structure in Fig. 8(a)). Such a spatial phase sequence was also reported in a diffusion experiment when BN was embedded into Ti matrix [34].

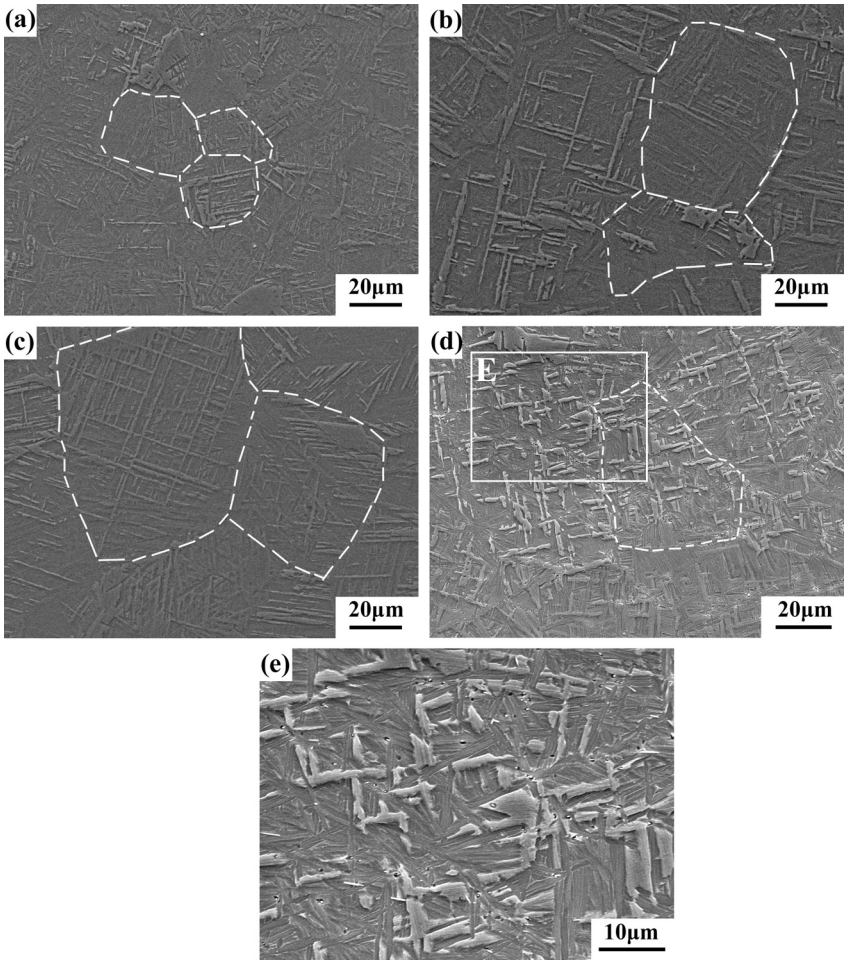

Fig. 13. SEM images of the SZ at different rotation rates: (a) 400 rpm, (b) 800 rpm, (c) 1200 rpm, (d) microstructure in the region where TiB wear particles existed in 1200 rpm FSP sample, and (e) higher magnification of region E in (d).

(4) In reaction stage 3 (Fig. 14(d)), BN and TiB_2 disappeared. For some BN particles, as the time increased, BN was totally consumed by reacting with Ti to form TiB_2. Because of the diffusion of B atoms, TiB_2 was also consumed by its further reaction with Ti. Therefore, finally TiB and α-Ti (N) were left (the second type of core–shell structure in Fig. 8(b)). Due to the "stirring" effect of the tool, TiB particles flowed into the matrix, and therefore only α-Ti (N) was left in some cases (the third type of core–shell structure in Fig. 8(a)).

4.3. The effect of tool wear on microstructure at the plunge point

Obviously different microstructures with wear products were observed in the 0 mm specimens for various tool rotation rates (Figs. 3(b), 5(a) and 7(e) and (8)). These phenomena were related to the change of β transus temperature because different contents of the wear product [N] atoms dissolved into the matrix (Fig. 15). As mentioned above, the peak FSP temperature at 1200 rpm probably exceeded 1300 °C but was lower than the melting temperature of Ti–6Al–4V (~1670 °C). In the "onion ring" region of the 1200 rpm–0 mm specimen, sufficient stirring effects made N be homogeneously dissolved into the matrix, leading to a low N concentration. EDS analysis showed that the contents of [N] in the "onion ring" were 0.7–2.7 at.%. When the temperature exceeded 1300 °C, material in the "onion ring" quickly entered to single phase β-Ti (N) field (marked with A in Fig. 15) and, after cooling down, transformed β-Ti (N) consisting of lamellar α-Ti (N) + residual β-Ti (N) was left. Based on the discussion above, it can be concluded that the BN core–shell structure in the "onion ring" contained four layers, that is, BN core, TiB_2 layer, TiB layer and transformed β-Ti(N) layer (the matrix).

It was reported that the tool wear was more prominent on the advancing side (AS) [35]. Therefore, in the "tail band" on the AS, due to a weaker stirring effect and greater tool wear than in the "onion ring", a higher solution of N in α-Ti could be achieved (EDS analysis showed that the contents of [N] were 5.0–19.1 at.%), which led to the stable existence of α-Ti (N), marked with B in Fig. 15. Therefore, the spatial phase sequences in the "tail band" and the "onion ring" region around BN particles in the 1200 rpm–0 mm specimen at high temperature during FSP were BN–TiB_2–TiB–α-Ti (N) and BN–TiB_2–TiB–β-Ti (N), respectively. Similarly, at the bottom region of

Table 1
Vickers hardness of different regions in the FSP samples at different rotation rates (HV).

Samples	BM	HAZ	TMAZ	SZ	Wear region
400 rpm	321 ± 2	285 ± 5	282 ± 4	332 ± 4	/
800 rpm		280 ± 5	284 ± 4	319 ± 9	337 ± 6
1200 rpm		287 ± 11	287 ± 1	323 ± 8	341 ± 8

Table 2
Tensile property of BM and FSP samples at different rotation rates.

	BM	400	800	800-wear	1200	1200-wear
UTS, MPa	1114 ± 11	1099 ± 5	1082 ± 28	1118 ± 16	1083 ± 26	1116 ± 37
Elongation, %	17.3 ± 2.8	14.4 ± 1.4	16.4 ± 2.3	13.1 ± 1.5	14.7 ± 2.3	10.0 ± 1.0

the SZ in the 400 rpm–0 mm specimen, [N] dissolved into the matrix, making material enter in the α + β phase field during FSP, marked with C in Fig. 15, and then cooled down to form a bimodal microstructure (Fig. 3(b)).

It should be pointed out that the [N] concentration in the 1200 rpm–0 mm specimen by EDS measurement was just for reference, which was inaccurate to express the [N] concentration during FSP because of two reasons. One is that the measurement in the content of light elements such as C, N, and O by EDS is inaccurate. Another is that the content of [N] would change significantly when cooling down because of its different solubility at different temperatures (Fig. 15). However, the locations of the materials in different regions with tool wear in the phase diagram (A, B and C in Fig. 15) were rational because they were inferred based on the microstructure. Besides, in this study, Ti2N phase were found in the region with tool wear in the 1200 rpm–0 mm specimen (Fig. 9(d)). According to Fig. 15, however, Ti2N phase obviously could not exist above 1100 °C. Therefore, Ti2N probably precipitated during cooling because of significantly decreased solubility of N with decreasing the temperature.

4.4. Microstructure and mechanical properties at different rotation rates

When the tool wear reached a steady-state condition, cavities were evidently visible at the bottom of the SZ at 400 rpm, while no such defects were observed at 800 and 1200 rpm (Fig. 11). These defects should be the result of insufficient heat input and material flow. For all the rotation rates, the SZs consisted of fully transformed β (Fig. 13(a)–(c)), suggesting that the peak processing temperature at all rotation rates exceeded the β transus point (~1000 °C). Moreover, the mean size of prior β grains increased with the rotation rate. It is rational because higher rotation rate could produce higher peak temperature and longer exposure time at high temperature, and therefore β grains grew more rapidly without the retard of α phase after the tool passed away. Compared with the microstructure in the SZ where no tool wear was found, the bands with TiB particles consisted of more α variants and smaller size of α colonies (Fig. 13(d) and (e)). The microstructural change should be on the basis of the fact that TiB particles formed because of the reaction between the pcBN tool and Ti–6Al–4V workpiece at high temperature during FSP, which became the heterogeneous nucleation fields for α variants during cooling.

It was reported [1] that for the fully transformed β, the α colony size, limited by the prior β size, determines the effective slip length and thereby dominates the mechanical properties. Strength and ductility increase with decreasing the β grain size. For fully equiaxed microstructure, primary α size, determining the slip length, is the main factor governing mechanical properties. For the bimodal microstructure, the main parameters determining the mechanical properties are the β grain size (determining effective slip length) and alloy element partitioning effect. The alloy element partitioning effect exerts a negative effect on the strength of bimodal microstructure, which leads to a lower basic strength of bimodal structure as compared to the fully transformed structure. Fully equiaxed microstructure usually shows a higher ductility than the other two structures [1].

At all rotation rates, the HAZs or TMAZs of FSP samples, consisting of bimodal microstructure, showed lower hardness than the SZs (Table 1). It was the result that alloy element partitioning effect played a more obvious role than the β grain size, even though for the bimodal microstructure in the HAZ or TMAZ, the β grain sizes were much smaller than that in the SZ. At both 800 and 1200 rpm, the regions with wear products showed a higher hardness and tensile strength but a lower ductility than those without tool wear (Tables 1 and 2). This phenomenon should be attributed to the combination of brittle TiB particles and the dissolution of N element. Dispersed TiB particles increase strength through load transfer by shear lag mechanism; however they increase the strain incompatibility between brittle TiB particles and relatively ductile titanium alloy matrix, thereby reducing the ductility of the material [36]. It is well-known that the dissolution of interstitial elements such as O and N largely increases the strength but decreases the ductility of titanium alloys. Therefore, formation of TiB particles and dissolution of N element due to the reaction between BN and Ti led to an increment in tensile strength but a loss of ductility.

The present study indicated the feasibility of FSP of Ti–6Al–4V alloy over a large range of rotation rates using a pcBN tool. Based on the similar principle of FSW and FSP, at high rotation

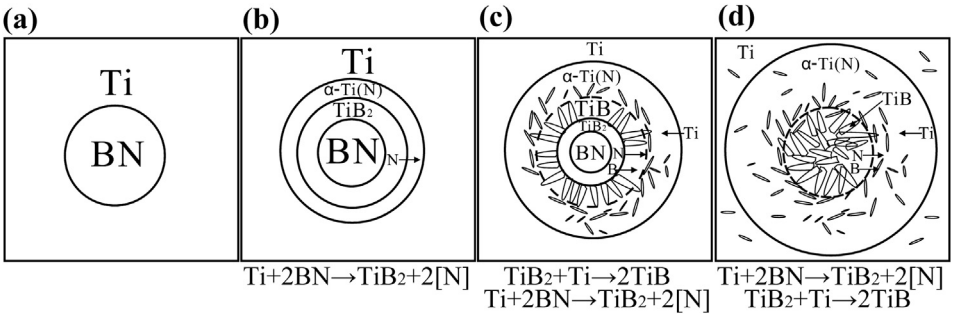

Fig. 14. Schematic diagram of the Ti-BN reaction process: (a) the initial stage, (b) reaction stage 1 with the formation of TiB_2 and α-Ti (N) layers, (c) reaction stage 2 with the formation of a TiB layer, and (d) reaction stage 3 with BN disappearing.

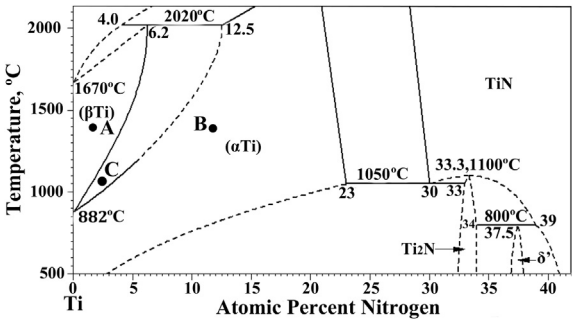

Fig. 15. Partial Ti–N phase diagram. A, B, and C represented the locations of the materials in the "onion ring", "tail band" of the 1200 rpm–0 mm specimen, and at the bottom region of the SZ with tool wear in the 400 rpm–0 mm specimen, in the phase diagram respectively.

rates (over 800 rpm) defects-free FSW Ti–6Al–4V joints are expected to be obtained using a pcBN tool. Unfortunately, under all conditions, tool wear occurred and it led to the loss of ductility of the SZ. Therefore, pcBN is probably not a good choice as a tool material for the FSW/FSP of titanium alloys, although it is proper for the FSW/FSP of steel. One of the main aspects for the FSW/FSP of titanium alloys in the future is still to seek for high wear-resistance tool materials, such as Co-based alloys [37] or to exploit a new tool by combine the advantages of both pcBN and W–Re alloys.

5. Conclusions

1. At higher rotation rates of 800 and 1200 rpm, the greatest tool wear occurred at the tool plunge point. At a lower rotation rate of 400 rpm, the greatest tool wear occurred at the location 7 mm from the tool plunge point.
2. At the tool plunge point at 1200 rpm, an "onion ring" structure formed because of the variations of the distribution of TiB particles. Spatial phase sequences around BN particles in the "tail band" and the "onion ring" region during FSP were BN–TiB_2–TiB–α-Ti (N) and BN–TiB_2–TiB–β-Ti (N), respectively, which were all the reaction products between BN and Ti.
3. At the plunge point, the dissolution of N atoms resulting from reaction between BN and Ti, led to different microstructures at different rotation rates: a bimodal microstructure at 400 rpm, a Widmanstatten microstructure in the "onion ring" region and a disc-shaped microstructure in the "tail band" at 1200 rpm.
4. At all the rotation rates, fully transformed β microstructures in the SZs were obtained. The mean grain size of the prior β grains increased with the rotation rate.
5. Tool wear products – TiB particles and α-Ti (N) led to the increment in hardness and strength but the loss of ductility of the SZs.

Acknowledgments

This work was supported by the National Natural Science Foundation of China under grant No. 51331008. The authors gratefully acknowledge Mr. X.C. Liu for the experimental help.

References

[1] G. Lütjering, J.C. Williams, Titanium, second ed., Springer, New York, 2007.
[2] R.S. Mishra, Z.Y. Ma, Mater. Sci. Eng. R 50 (2005) 1–78.
[3] C.Z. Zhou, X.Q. Yang, G.H. Luan, Mater. Chem. Phys. 98 (2006) 285–290.
[4] T.W. Nelson, J.Q. Su, R. Mishra, M. Mahoney, Acta Mater. 51 (2003) 713–729.
[5] G.M. Xie, Z.Y. Ma, L. Geng, Mater. Sci. Eng. A 486 (2008) 49–55.
[6] S.S. Di, X.Q. Yang, D.P. Fang, G.H. Luan, Mater. Chem. Phys. 104 (2007) 244–248.
[7] L. Litynska, R. Braun, G. Staniek, C.D. Donne, J. Dutkiewicz, Mater. Chem. Phys. 81 (2003) 293–295.
[8] L. Zhou, H.J. Liu, P. Liu, Q.W. Liu, Scr. Mater. 61 (2009) 596–599.
[9] H.J. Liu, L. Zhou, Q.W. Liu, Mater. Des. 31 (2010) 1650–1655.
[10] P. Edwards, M. Ramulu, Sci. Technol. Weld. Joining 14 (2009) 669–680.
[11] L. Fratini, F. Micari, G. Buffa, V.F. Ruisi, CIRP Ann. Manuf. Technol. 59 (2010) 271–274.
[12] A.L. Pilchak, W. Tang, H. Sahiner, A.P. Reynolds, J.C. Williams, Metall. Mater. Trans. A 42 (2011) 745–762.
[13] A.L. Pilchak, M.C. Juhas, J.C. Williams, Metall. Mater. Trans. A 38 (2007) 401–408.
[14] Y. Zhang, Y.S. Sato, H. Kokawa, S.H.C. Park, S. Hirano, Mater. Sci. Eng. A 485 (2008) 448–455.
[15] W.B. Lee, C.Y. Lee, W.S. Chang, Y.M. Yeon, S.B. Jung, Mater. Lett. 59 (2005) 3315–3318.
[16] J. Angseryd, H.O. Andren, Wear 271 (2011) 2610–2618.
[17] K. Hirosaki, K. Shintani, H. Kato, F. Asakura, K. Matsuo, JSME Int. J. Ser. C 47 (2004) 14–20.
[18] Y.S. Sato, H. Yamanoi, H. Kokawa, T. Furuhara, Scr. Mater. 57 (2007) 557–560.
[19] W.M. Thomas, P.L. Threadgill, E.D. Nicholas, Sci. Technol. Weld. Joining 4 (1999) 365–372.
[20] M. Matsushita, Y. Kitani, R. Ikeda, M. Ono, H. Fujii, Y.D. Chung, Sci. Technol. Weld. Joining 16 (2011) 181–187.
[21] Y. Zhang, Y.S. Sato, H. Kokawa, S.H.C. Park, S. Hirano, Mater. Sci. Eng. A 488 (2008) 25–30.
[22] S. Park, Y. Sato, H. Kokawa, K. Okamoto, S. Hirano, M. Inagaki, Metall. Mater. Trans. A 40 (2009) 625–636.
[23] A. Steuwer, S.J. Barnes, J. Altenkirch, R. Johnson, P.J. Withers, Metall. Mater. Trans. A 43 (2012) 2356–2365.
[24] A.V. Kartavykh, V.V. Tcherdyntsev, J. Zollinger, Mater. Chem. Phys. 119 (2010) 347–350.
[25] A.H. Feng, B.L. Xiao, Z.Y. Ma, Compos. Sci. Technol. 68 (2008) 2141–2148.
[26] B.J. Kooi, Y.T. Pei, J.T.M. De Hosson, Acta Mater. 51 (2003) 831–845.
[27] L. Zhou, H.J. Liu, P. Liu, Trans. China Weld. Inst. (Chin. Ed.) 30 (2009) 93–97.
[28] D.J. Shindo, A.R. Rivera, L.E. Murr, J. Mater. Sci. 37 (2002) 4999–5005.
[29] K.N. Krishnan, Mater. Sci. Eng. A 327 (2002) 246–251.
[30] Q. Yang, B.L. Xiao, Z.Y. Ma, Metall. Mater. Trans. A 43 (2012) 2094–2109.
[31] R. Fonda, A. Reynolds, C.R. Feng, K. Knipling, D. Rowenhorst, Metall. Mater. Trans. A 44 (2013) 337–344.
[32] N. Tikekar, Novel Double-layer Titanium Boride (TiB_2 + TiB) Coating on CP-Ti and Ti–6Al–4V Alloy: Kinetics of Boron Diffusion and Coating Morphologies (Doctoral dissertation), University of Utah, 2007, p. 38.
[33] N.M. Tikekar, K.S.R. Chandran, A. Sanders, Scr. Mater. 57 (2007) 273–276.
[34] E. Faran, I. Gotman, E.Y. Gutmanas, Mater. Sci. Eng. A 288 (2000) 66–74.
[35] A.L. Pilchak, M.C. Juhas, J.C. Williams, Metall. Mater. Trans. A 38 (2007) 435–437.
[36] L.G. Huang, F.T. Kong, Y.Y. Chen, S.L. Xiao, Mater. Sci. Eng. A 560 (2013) 140–147.
[37] Y.S. Sato, Y. Nagahama, S. Mironov, H. Kokawa, S.H.C. Park, S. Hirano, Scr. Mater. 67 (2012) 241–244.